OPEN ACCESS
IOP Publishing
Journal of Physics G: Nuclear and Particle Physics
J. Phys. G: Nucl. Part. Phys. **50** (2023) 025103 (25pp)
https://doi.org/10.1088/1361-6471/aca923

# Halo EFT for $^{31}$Ne in a spherical formalism

**Wael Elkamhawy**[1,2] **and Hans-Werner Hammer**[1,2,3]

[1] Technische Universität Darmstadt, Department of Physics, Institut für Kernphysik, 64289 Darmstadt, Germany
[2] Helmholtz Forschungsakademie Hessen für FAIR (HFHF), GSI Helmholtzzentrum für Schwerionenforschung GmbH, 64291 Darmstadt, Germany
[3] ExtreMe Matter Institute EMMI, GSI Helmholtzzentrum für Schwerionenforschung GmbH, 64291 Darmstadt, Germany

E-mail: elkamhawy@theorie.ikp.physik.tu-darmstadt.de and Hans-Werner.Hammer@physik.tu-darmstadt.de

Received 19 July 2022, revised 19 November 2022
Accepted for publication 6 December 2022
Published 29 December 2022

**Abstract**

We calculate the electromagnetic properties of the deformed one-neutron halo candidate $^{31}$Ne using Halo effective field theory (Halo EFT). In this framework, $^{31}$Ne is bound via a resonant $P$-wave interaction between the $^{30}$Ne core and the valence neutron. We set up a spherical formalism for $^{31}$Ne in order to calculate the electromagnetic form factors and the E1-breakup strength distribution into the $^{30}$Ne-neutron continuum at leading order in Halo EFT. The associated uncertainties are estimated according to our power counting. In particular, we assume that the deformation of the $^{30}$Ne core enters at next-to-leading order. It can be accounted for by including the $J^P = 2^+$ excited state of $^{30}$Ne as an explicit field in the effective Lagrangian.

Keywords: Halo EFT, Coulomb dissociation, $P$-wave neutron halo, Electromagnetic structure

(Some figures may appear in colour only in the online journal)

## 1. Introduction

The emergence of halo nuclei is an intriguing aspect of atomic nuclei near the driplines [1–3]. They were discovered in the 1980s at radioactive beam facilities and are characterized by an unusually large interaction radius [4]. Nuclear halo states consist of a tightly bound core with

a characteristic size $\sim 1/M_{\rm hi}$ and a cloud of halo nucleons of size $\sim 1/M_{\rm lo}$, which is much larger than neighbouring isotopes. The large separation between the momentum scales $M_{\rm hi} \gg M_{\rm lo}$ leads to universal properties, which are independent of the details of the core [5–7]. These properties are most pronounced in neutron halos as they are not affected by the long-range Coulomb repulsion between charged particles.

The separation of scales in halo nuclei can formally be exploited using Halo effective field theory (Halo EFT) [8, 9] (see [7] for a recent review). It uses effective degrees of freedom and allows to describe observables in a systematic expansion in $M_{\rm lo}/M_{\rm hi}$, thus enabling uncertainty estimates based on the expected size of higher-order terms in the expansion. For the dynamics of the halo nucleons, the substructure of the core can be considered short-distance physics that is not resolved, although low-lying excited states of the core sometimes have to be included explicitly. One assumes the core to be structureless and treats the nucleus as a few-body system of the core and the valence nucleons. Corrections from the core structure appear at higher orders in the EFT expansion, and can be accounted for in perturbation theory. Since the relevant halo scale $M_{\rm lo}$ is small compared to the pion mass, even the pion exchange interaction between nucleons and/or the nuclear core is not resolved. Thus, halos can be described by an EFT with short-range contact interactions. In chiral effective field theories, which have a higher breakdown scale $M_{\rm hi}$, the long-distance structure of the halo wave function emerges from a combination of explicit pion exchange and short-range contact interactions (see [10–12] for reviews). However, the precise contribution of contact terms and pion exchange is resolution-dependent and thus not observable. A new facet in halo nuclei compared to few-nucleon systems is the appearance of resonant interactions in higher partial waves [8, 9]. However, there are many light halo nuclei where $S$-wave interactions are dominant.

The fact that the halo neutrons and the core are treated independently in Halo EFT means that the halo neutrons are not antisymmetrized with neutrons in the core—the latter are not active degrees of freedom in the EFT. However, the contribution of a hypothetical configuration where a neutron from the core and one from the halo are exchanged to an observable is governed by the overlap of the wave functions of the core and the halo. Since the ranges of the core and halo wave functions are $1/M_{\rm hi}$ and $1/M_{\rm lo}$, respectively, the size of this contribution is determined by the standard Halo EFT expansion in $M_{\rm lo}/M_{\rm hi}$. Therefore, within the domain of applicability of Halo EFT the impact of anti-symmetrization on observables is controlled and can be incorporated together with that of other short-distance effects. In a single-neutron halo, these effects enter through the low-energy constants of the nucleon-core interaction which is fitted to experimental data or *ab initio* input. In a two-neutron halo, they also enter through a short-range three-body force. This can be understood as follows [7]: the full anti-symmetrization of the wave function in a theory with active core neutrons will result in additional nodes of the halo wave function since some neutrons must be in excited states to obey the Pauli principle. In a cluster model, these additional nodes are generated by including deep unphysical bound states (ghost states) of the core and the halo. In Halo EFT such deep unphysical states are not included explicitly. The manifestation of the corresponding physics in Halo EFT can be understood by assuming that the unphysical states have been integrated out of the theory. This generates a short-range three-body force between the core and the two halo neutrons (or modifies an already existing three-body force in the theory).

This strategy was, for example, used in [13] to describe the breakup of $^{11}$Be in peripheral collisions on Pb and C targets. The calculation demonstrated that a good description of the Coulomb-dominated breakup on Pb at energies up to about 2 MeV can be obtained, independent of the short-distance part of the halo wave function. The nuclear-dominated breakup on C, however, was found to be more sensitive to short-range physics. In a similar way, the

effects of virtual excitation of the $^{11}$Be core can be captured by an effective three-body force [14] or by including the excited states explicitly [15].

In heavier halo nuclei in the region $Z = 9-12$, the structure of the ground state is believed to be more complicated and deformed halos are expected. Nakamura and collaborators provided the first indications of a halo structure in $^{31}$Ne [16]. Subsequently, they showed that the ground state of $^{31}$Ne has a low one-neutron separation energy and is a deformed $P$-wave halo [17]. A similar structure was found for $^{37}$Mg [18] which is even heavier. In the case of $^{31}$Ne, they used state-of-the-art shell model calculations to analyze nuclear and electromagnetic 1$n$-removal reactions on C and Pb targets and found that the weakly-bound $P$-wave neutron carries only about 30% of the single-particle strength. The first excitation energy of the $^{30}$Ne core is 800 keV above the ground state which has spin and parity quantum numbers $J^P = 0^+$. Meanwhile, the quantum numbers of $^{31}$Ne are $J^P = 3/2^-$ with a neutron separation energy of 150 keV.

The possibility that $^{31}$Ne could be a one-neutron halo was suggested in theoretical work using density-dependent relativistic mean-field theory [19]. Various authors have analyzed the experimental data on Coulomb dissociation of $^{31}$Ne based on this assumption [20, 21]. Urata *et al* showed that the data can be well reproduced in the particle-rotor model when the quadrupole deformation parameter of the $^{30}$Ne core is around $\beta_2 = 0.2...0.3$ [21]. The preferred structure of a $P$-wave neutron halo with $J^P = 3/2^-$ was also obtained using a microscopic $G$-Matrix calculation [22] and a deformed WoodsSaxon potential for the neutron-core interaction [23]. A theoretical analysis of the ground state quantum numbers $^{31}$Ne based on experimental data on Coulomb breakup and neutron removal reached the same conclusion [24]. Most recently, the Gamow shell model was applied to the neon isotopes $^{26}$Ne−$^{31}$Ne [25]. This study confirmed the $P$-wave neutron halo character of $^{31}$Ne and suggested that $^{29}$Ne could also be a neutron halo.

The separation of scales in $^{31}$Ne allows for a controlled, systematic description of its properties using Halo EFT. A first Halo EFT calculation of the electric properties of $^{31}$Ne based on the general framework of [26] was carried out in [27]. In this paper, we present a complete discussion of the electromagnetic structure of $^{31}$Ne, as well as its E1 breakup. We describe $^{31}$Ne as a $P$-wave $^{30}$Ne-neutron bound state. The deformation of the $^{30}$Ne core enters at next-to-leading order and can be calculated by including the $J^P = 2^+$ excited state as an explicit field in the effective Lagrangian. Instead of using the standard Cartesian formulation of the field theory applied in [27], we introduce a spherical basis that is ideally suited for the description of halo nuclei beyond the $S$-wave. It employs the correct number of field components in a given partial wave and thus does not require any auxilliary conditions, leading to more compact and transparent expressions. Moreover, we also calculate magnetic observables.

In section 2, we present the Halo EFT for $^{31}$Ne in a spherical basis, derive the $^{30}$Ne-neutron scattering amplitude, and discuss the corresponding power counting. The electromagnetic (EM) sector is discussed in section 3. We incorporate EM interactions and derive the scalar and vector currents and their corresponding form factors. In section 4, we extract the leading moments from the form factors and discuss universal correlations between them. Moreover, we elucidate the implications of the multipole moments with respect to the deformation of $^{31}$Ne and determine the quadrupolar deformation parameter $\beta_2$. The E1 breakup of $^{31}$Ne into the $^{30}$Ne-neutron continuum is analyzed in section 5. In passing, we note that the inverse process of E1 neutron capture into the $P$-wave neutron halo $^8$Li was previously considered using Halo EFT in [28–30]. Finally, we present our conclusions in section 6.

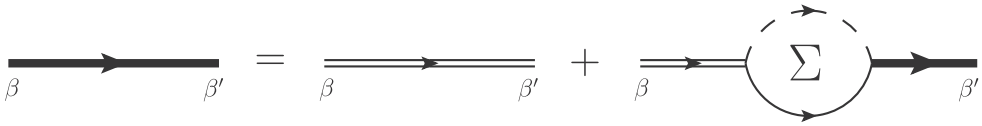


**Figure 1.** Dyson equation for the full dimer propagator. The thick line denotes the full dimer propagator, while the double solid line denotes the bare propagator. The single solid line represents the neutron field, whereas the dashed line represents the core field.

## 2. Halo EFT for $^{31}$Ne

### 2.1. Lagrangian: strong sector

We describe $^{31}$Ne as a shallow $P$-wave bound state of the $^{30}$Ne core and the valence neutron. Our effective Lagrangian includes a bosonic field $c$ with $J^P = 0^+$ for the $^{30}$Ne core and a $J^P = 1/2^+$ spinor field $n_\alpha$ with $\alpha \in \{-1/2,\ 1/2\}$ for the neutron. Moreover, a $J^P = 3/2^-$ dimer field $\pi_\beta$ with $\beta \in \{-3/2,\ -1/2,\ 1/2,\ 3/2\}$ captures the physics of $^{31}$Ne and the core-neutron continuum. The corresponding Lagrangian is given by[4]

$$\mathscr{L} = c^\dagger\left[i\partial_0 + \frac{\nabla^2}{2m_c}\right]c + n_\alpha^\dagger\left[i\partial_0 + \frac{\nabla^2}{2m_n}\right]n_\alpha + \pi_\beta^\dagger\left[\eta_1\left(i\partial_0 + \frac{\nabla^2}{2M_{nc}}\right) + \Delta_1\right]\pi_\beta$$
$$- g_1[(c^\dagger \overleftrightarrow{\nabla_i} n_\alpha^\dagger)\pi_\beta\, C^{\frac{3}{2}\beta}_{(1i)(\frac{1}{2}\alpha)} + \text{H.c.}], \tag{1}$$

where $M_{nc} \equiv m_n + m_c$ denotes the kinetic mass of the core-neutron system, $\Delta_1$ and $g_1$ are coupling constants, while $\eta_1 \equiv \pm 1$ is a sign to be determined from matching to scattering observables. Moreover, $\overleftrightarrow{\nabla} \equiv m_R[{m_c}^{-1}\overleftarrow{\nabla} - {m_n}^{-1}\overrightarrow{\nabla}]$ is the Galilean-invariant derivative where $m_R = m_c m_n/(m_c + m_n)$ denotes the core-neutron reduced mass. The coefficient $C^{\frac{3}{2}\beta}_{(1i)(\frac{1}{2}\alpha)}$ is a Clebsch–Gordan coefficient coupling the neutron spin and the core-neutron relative angular momentum to the total spin $J = 3/2$ of the dimer field. Note that the index $i$ of the derivative operator is a spherical index denoting the projection of the $P$-wave interaction whereas $\alpha$ and $\beta$ are spinor indices denoting the projections of their corresponding spins. Moreover, we use spherical coordinates throughout this work. Our conventions are summarized in appendix A.

### 2.2. Full dimer propagator

For convenience, we use the power divergence subtraction scheme from [31] and [32] with renormalization scale $\mu$. In order to determine the full dimer propagator, we dress the bare propagator

$$iD^0(p_0, \boldsymbol{p}) = \frac{i}{\eta_1\left(p_0 - \frac{\boldsymbol{p}^2}{2M_{nc}}\right) + \Delta_1 + i\epsilon} \tag{2}$$

with dimer self-energies. We end up with the Dyson equation which is depicted diagramatically in figure 1. This geometric series represents the exact solution to the core-neutron problem.

The dimer self-energy is diagonal in the spin indices of the incoming and outgoing dimer fields and reads

[4] We use natural units with $\hbar = c = 1$ throughout this work.

$$-i\Sigma_{\beta'\beta}(p_0, \boldsymbol{p}) = -i\Sigma(p_0, \boldsymbol{p})\delta_{\beta'\beta}, \tag{3}$$

with

$$-i\Sigma(p_0, \boldsymbol{p}) = \frac{im_R {g_1}^2 2m_R\left(p_0 - \frac{\boldsymbol{p}^2}{2M_{nc}}\right)}{6\pi}\left(\frac{3}{2}\mu - \sqrt{-2m_R\left(p_0 - \frac{\boldsymbol{p}^2}{2M_{nc}}\right) - i\epsilon}\right). \tag{4}$$

Since the $\Sigma_{\beta'\beta}$ and $D^0(p_0, \boldsymbol{p})$ are diagonal in the spin indices, the full dimer propagator is also diagonal and reads

$$iD_{\beta'\beta}(p_0, \boldsymbol{p}) = iD(p_0, \boldsymbol{p})\delta_{\beta'\beta}, \tag{5}$$

where the scalar full propagator is given by

$$\begin{aligned} iD(p_0, \boldsymbol{p}) &= \frac{iD^0(p_0, \boldsymbol{p})}{1 - \Sigma(p_0, \boldsymbol{p})D^0(p_0, \boldsymbol{p})} \\ &= \frac{i}{\eta_1\left(p_0 - \frac{\boldsymbol{p}^2}{2M_{nc}}\right) + \Delta_1 - \Sigma(p_0, \boldsymbol{p}) + i\epsilon}. \end{aligned} \tag{6}$$

The full dimer propagator must have a simple pole at the energy $p_0 = \frac{p^2}{2M_{nc}} - B_1$ with $B_1 = \gamma_1^2/(2m_R)$ the one-neutron separation energy of $^{31}$Ne, whereas $\gamma_1 > 0$ is the corresponding binding momentum. In order to calculate $^{31}$Ne observables, we need the wave function renormalization constant defined by

$$Z_\pi^{-1} = \left(\frac{\partial}{\partial p_0}\frac{1}{D(p_0, \boldsymbol{p})}\right)\Bigg|_{p_0 = \frac{\boldsymbol{p}^2}{2M_{nc}} - B_1}, \tag{7}$$

which yields

$$Z_\pi = -\frac{6\pi}{m_R^2 {g_1}^2}\frac{1}{3\gamma_1 - \frac{6\pi\eta_1}{m_R^2 {g_1}^2} - 3\mu}. \tag{8}$$

### 2.3. Scattering amplitude and matching

The $P$-wave neutron-core scattering amplitude in the $J = 3/2$-channel is obtained by attaching external core and neutron lines to the full dimer propagator from equation (6), see figure 2. In the center-of-mass frame with $E = p^2/(2m_R) = p'^2/(2m_R)$ and $p = |\boldsymbol{p}| = |\boldsymbol{p}'|$, it reads

$$T_{\alpha'\alpha}(\boldsymbol{p}', \boldsymbol{p}) = \frac{6\pi}{m_R}\frac{\frac{2}{3}\boldsymbol{p}' \cdot \boldsymbol{p}\,\delta_{\alpha'\alpha} - \frac{i}{3}(\boldsymbol{\sigma} \cdot (\boldsymbol{p}' \times \boldsymbol{p}))_{\alpha'\alpha}}{\left(\frac{6\pi\Delta_1}{m_R {g_1}^2} + \frac{3\pi\eta_1}{m_R^2 {g_1}^2}p^2 + \frac{3}{2}\mu p^2 + ip^3\right)}, \tag{9}$$

where $\boldsymbol{\sigma}$ is the three-dimensional vector with the Pauli matrices as its components. The corresponding result for a $J = 1/2$ state is given in appendix B.

Comparing equation (9) to the general form of the amplitude in terms of the $P$-wave effective range parameters

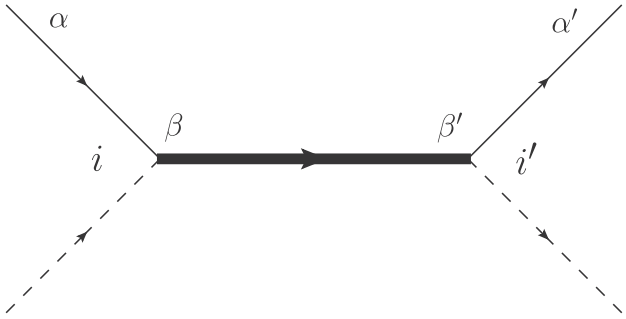


**Figure 2.** Pictorial representation of the neutron-core scattering amplitude including spin indices. The thick line denotes the full dimer propagator, the single solid line represents the neutron field, and the dashed line represents the core field.

$$T_{\alpha'\alpha}(\boldsymbol{p}', \boldsymbol{p}) = \frac{6\pi}{m_R} \frac{\frac{2}{3}\boldsymbol{p}' \cdot \boldsymbol{p}\, \delta_{\alpha'\alpha} - \frac{i}{3}(\boldsymbol{\sigma} \cdot (\boldsymbol{p}' \times \boldsymbol{p}))_{\alpha'\alpha}}{\left(\frac{1}{a_1} - \frac{1}{2}r_1 p^2 + ip^3\right)}, \tag{10}$$

we obtain the matching conditions

$$a_1 = \frac{m_R g_1^{\,2}}{6\pi\Delta_1}, \quad r_1 = -\frac{6\pi\eta_1}{m_R^2 g_1^{\,2}} - 3\mu, \tag{11}$$

where $a_1$ is the scattering volume while $r_1$ denotes the $P$-wave effective momentum. These parameters can be determined directly from scattering, but they can also be determined from matching to bound state properties using the relations derived below. Since the parameter $r_1$ has to be negative for causal scattering [33, 34], the sign $\eta_1$ is determined to be $\eta_1 = +1$ according to equation (11). With these matching conditions, the wave function renormalization constant reads

$$Z_\pi = -\frac{6\pi}{m_R^2 g_1^{\,2}} \frac{1}{3\gamma_1 + r_1}. \tag{12}$$

$Z_\pi$ is the residue of the bound state pole at the energy $p_0 = p^2/(2M_{nc}) - \gamma_1^2/(2m_R)$ in the full dimer propagator where $\gamma_1$ is a real positive solution to the equation

$$\frac{1}{a_1} + \frac{r_1}{2}\gamma_1^2 + \gamma_1^3 = 0. \tag{13}$$

The corresponding bound state pole conditions for an $S$- and $D$-wave halo nucleus at leading order can be found in [26, 35], respectively. They read

$$\frac{1}{a_0} - \gamma_0 = 0, \tag{14}$$

$$\frac{1}{a_2} + \frac{r_2}{2}\gamma_2^2 + \frac{\mathscr{P}_2}{4}\gamma_2^4 = 0, \tag{15}$$

where $a_0$ and $a_2$, $r_2$, $\mathscr{P}_2$ are the corresponding effective range parameters while $\gamma_0$ and $\gamma_2$ are the corresponding binding momenta. Note that the number of effective range parameters required at leading order depends on the power counting and, in general, is different in different partial waves.

### 2.4. Power counting

Following [9], we assume only one combination of coupling constants to be fine-tuned, namely $\Delta_1/g_1^2$. This is sufficient in order to produce a shallow $P$-wave bound state. With this choice, the scattering volume $a_1$ is enhanced by

$$a_1 \sim \frac{1}{M_{\rm lo}^2 M_{\rm hi}}, \tag{16}$$

whereas the $P$-wave effective momentum $r_1$ scales like

$$-r_1 \sim M_{\rm hi}, \tag{17}$$

where $M_{\rm lo}$ and $M_{\rm hi}$ denote the typical low- and high-momentum scales of the system, respectively. The low-momentum scale is given by the binding momentum of the shallow $P$-wave bound state. In the case of $^{31}$Ne with a binding energy of $B_1 = 150$ keV [17], this yields[5]

$$M_{\rm lo} \approx \gamma_1 = \sqrt{2m_R B_1} = 16.5 \text{ MeV}. \tag{18}$$

The high-momentum scale can be approximated by the breakdown scale of the theory. Since we do not include the $J^P = 2^+$ state of the $^{30}$Ne core explicitly, $M_{\rm hi}$ can be estimated by the associated momentum scale of the excitation energy $E_{\rm ex} = 792$ keV [36]. The corresponding value is given by $M_{\rm hi} \approx \sqrt{2m_R E_{\rm ex}} \approx 40$ MeV. At this momentum scale, the deformation of the $^{30}$Ne core due to this excited state starts to play a role.

Given this power counting scheme, the equation for the pole position, equation (13), and the wave function renormalization, equation (12), can be expanded at leading order in $M_{\rm lo}/M_{\rm hi}$ to yield

$$\gamma_1 = \sqrt{-\frac{2}{a_1 r_1}} \quad \text{and} \quad Z_\pi^{\rm LO} = -\frac{6\pi}{m_R^2 g_1^2 r_1}. \tag{19}$$

The quantity $g_1^2 Z_\pi^{\rm LO}$ is proportional to the absolute value squared of the EFT wave function at the bound state pole. Thus, $Z_\pi$ must be positive. As a consequence, $r_1$ must be negative. At NLO, the wave function renormalization is given by the expression from equation (12)

$$Z_\pi^{\rm NLO} = -\frac{6\pi}{m_R^2 g_1^2} \frac{1}{3\gamma_1 + r_1}. \tag{20}$$

Thus, only if $|r_1| > 3\gamma_1$ holds, we end up with a normalizable state with positive residue. This requirement is consistent with the hierarchy $M_{\rm lo} \ll M_{\rm hi}$ which forms the basis of our power counting.

For a shallow $P$-wave state, we have at least two effective range expansion parameters, $a_1$ and $r_1$, which have to be fixed by observables. Until now, we only know the neutron separation energy of $^{31}$Ne from the experiment, which is not enough in order to fix both effective range expansion parameters. Therefore, we will estimate the $P$-wave effective momentum $r_1$ in an interval around the breakdown scale, according to equation (17), and use the neutron separation energy to determine the scattering volume $a_1$. Based on these assumptions we can calculate other observables accessible in our theory, such as the electromagnetic current and the corresponding multipole moments as well as the associated radii.

[5] Since we work in Halo EFT, the binding energy corresponds to the neutron separation energy of the halo nucleus.

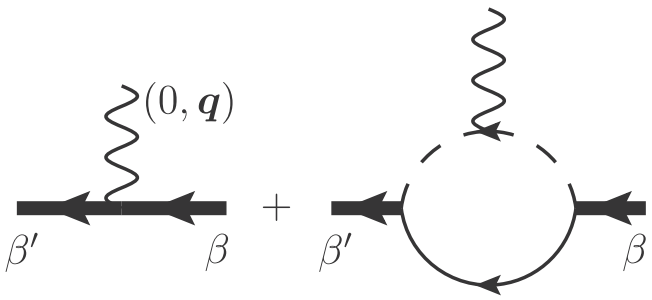


**Figure 3.** Diagrams contributing to the irreducible vertex for an $A_0$ photon coupling to the $^{30}$Ne-$n$ $P$-wave bound state at LO.

Taking everything together, we estimate

$$r_1 \sim M_{\rm hi} \in [-150,\ -50]\ \text{MeV}. \tag{21}$$

Values of $r_1$ in this interval are consistent with unitarity and the estimated breakdown scale of our theory associated with the $J^P = 2^+$ excited state of the core.

## 3. Electromagnetic sector

We now go on to include electromagnetic interactions in the effective theory. Moreover, we derive the corresponding form factors using spherical coordinates. We present results for the form factors of $^{31}$Ne and provide general expressions for form factors of arbitrary multipolarity $L$.

In the first step, electromagnetic interactions are included via minimal substitution

$$\partial_\mu \to D_\mu = \partial_\mu + ie\hat{q}A_\mu, \tag{22}$$

meaning that the usual derivative $\partial_\mu$ in the Lagrangian in equation (1) is replaced by the covariant derivative $D_\mu$ containing the charge operator $\hat{q}$, the elementary charge $e > 0$ and the photon field $A^\mu = (A_0, \boldsymbol{A})$. We use the Heaviside–Lorentz convention where the fine-structure constant is given by $\alpha = e^2/(4\pi)$. In the second step, all possible gauge-invariant operators involving the electric field $\boldsymbol{E}$ and also the magnetic field $\boldsymbol{B}$ have to be considered within our power counting scheme. It turns out that only gauge-invariant operators proportional to the magnetic field $\boldsymbol{B}$ are contributing at LO whereas operators involving the electric field $\boldsymbol{E}$ contribute at higher orders.

### 3.1. Scalar current

First, we calculate the matrix element of the zeroth component of the electromagnetic current of $^{31}$Ne. Therefore, we consider the amplitude with an irreducible vertex for an $A_0$ photon with four-momentum $(0, \boldsymbol{q})$ coupling to the $^{30}$Ne-$n$ $P$-wave bound state with initial momentum $\boldsymbol{p}$ and final momentum $\boldsymbol{p}'$. Thus, we have $\boldsymbol{q} = \boldsymbol{p}' - \boldsymbol{p}$ and define $q = |\boldsymbol{q}|$. The initial and final states are characterized by their momenta and projections of the spin, denoted by $|\pi_\beta(\boldsymbol{p})\rangle$ and $|\pi_{\beta'}(\boldsymbol{p}')\rangle$, respectively. The LO contributions to this amplitude are depicted in figure 3. Since $^{31}$Ne has a total spin of $3/2$, there are four possible projections for each, the initial and final state. Hence, the tensors connecting initial and final state projections are $4 \times 4$ matrices in spin space.

The scalar electromagnetic transition amplitude can be written as

$$\langle \pi_{\beta'}(\boldsymbol{p}')|\ J^0|\pi_\beta(\boldsymbol{p})\rangle = -\mathrm{i}q_c e G_{\mathrm{E0}}(q)\sqrt{\tfrac{4\pi}{1}}\,q^0 Y^*_{00}(\boldsymbol{e_q})(\widetilde{T}^{[00]}_{3/2})_{\beta'\beta} - i\mu_Q G_{\mathrm{E2}}(q)\tfrac{1}{2}\sqrt{\tfrac{4\pi}{5}}\,q^2\sum_M Y^*_{2M}(\boldsymbol{e_q})(\widetilde{T}^{[2M]}_{3/2})_{\beta'\beta}, \tag{23}$$

where $\boldsymbol{e_q}$ is the unit vector of $\boldsymbol{q}$, $q_c$ is the charge of the core in terms of the elementary charge $e$ and $\mu_Q$ is the quadrupole moment. Moreover, the electric monopole and quadrupole form factors are denoted by $G_{\mathrm{E0}}(q)$ and $G_{\mathrm{E2}}(q)$, respectively. Since the multipole moments are explicitly factored out of the form factors in equation (23), $G_{\mathrm{E0}}(q)$ and $G_{\mathrm{E2}}(q)$ are normalized to one in the limit of vanishing photon momentum by construction. The tensors $\tilde{T}^{00}_{3/2}$ and $\tilde{T}^{2M}_{3/2}$ are normalized $4\times 4$ polarization matrices [37]. For general $J$, they are $(2J+1)\times(2J+1)$ matrices given by

$$(\tilde{T}^{[LM]}_J)_{\beta'\beta} = \frac{C^{J\beta'}_{(J\beta)(LM)}}{C^{JJ}_{(JJ)(L0)}}. \tag{24}$$

They are normalized such that they have a coefficient of 1 for maximal projections. Consequently, the multipole moments are defined for maximal projections as it is usually done by convention. The subscript $J$ indicates the spin of the considered two-particle bound state, while $L$ stands for the angular momentum of the photon. The possible contributions for $L$ result from coupling the two $P$-wave spherical harmonics appearing in the right diagram of figure 3. Furthermore, $M$ denotes the projection of the angular momentum $L$. This implicit angular momentum coupling can yield contributions of the photon multipolarities $L=0,\,1,\,2$ in the electromagnetic transition amplitude, equation (23). Due to parity conservation, however, only even numbers of $L$ contribute so that we are left with $L\in\{0,\,2\}$. Hence, as we can read from equation (23), the electric monopole and quadrupole form factors with their corresponding multipole moments appear for $J=3/2$, but no dipole form factor.[6] The LO results for the electric form factors read

$$G_{\mathrm{E0}}(q) = \left[1 - \frac{\gamma_1}{r_1} + \frac{y^2q^2+2\gamma_1^2}{yqr_1}\arctan\left(\frac{yq}{2\gamma_1}\right)\right], \tag{25}$$

$$\mu_Q G_{\mathrm{E2}}(q) = -\frac{q_c e}{2r_1 yq^3}\left[2\gamma_1 yq + (y^2q^2-4\gamma_1^2)\arctan\left(\frac{yq}{2\gamma_1}\right)\right], \tag{26}$$

with

$$y = m_n/M_{nc} = m_R/m_c. \tag{27}$$

Since gauge invariance ensures charge conservation, the normalization $\lim_{q\to 0} G_{\mathrm{E0}}(q) = 1$ is automatically fulfilled and hence serves as a consistency check. The normalization condition $\lim_{q\to 0} G_{\mathrm{E2}}(q) = 1$ determines the quadrupole moment

$$\mu_Q = -\frac{y^2 q_c e}{3\gamma_1 r_1}. \tag{28}$$

[6] Note that if we would consider a spin $1/2$ dimer, there would be no quadrupole contribution in equation (23) because of the properties of the Clebsch–Gordan coefficients.

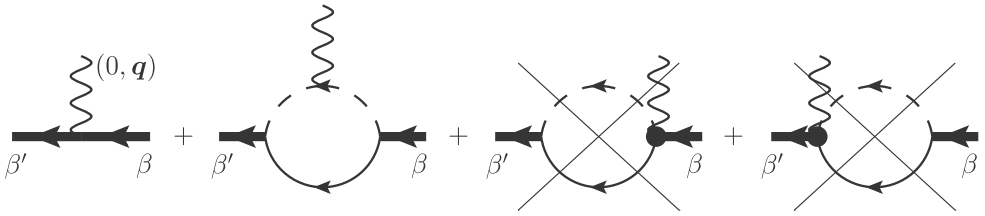


**Figure 4.** Diagrams contributing to the irreducible vertex for an $A_k$ photon coupling to the $^{30}$Ne-$n$ $P$-wave bound state at LO. The two diagrams on the right, which are crossed out, can be shown to vanish by parity conservation.

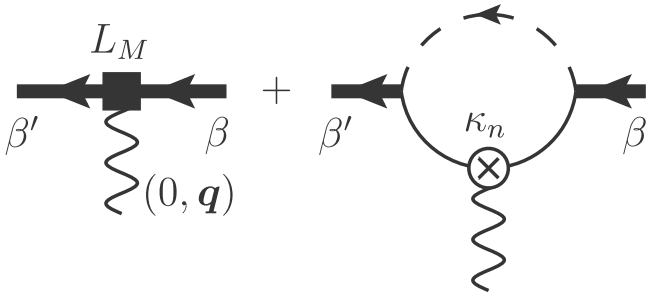


**Figure 5.** Diagrams contributing to the irreducible vertex for a $B_k$ photon coupling to the $^{30}$Ne-$n$ $P$-wave bound state at LO. On the one hand, the magnetic photon can couple to the neutron spin via the anomalous magnetic moment $\kappa_n$ and on the other hand, it can directly couple to the dimer spin via the counterterm $L_{\rm M}$.

Inserting this quadrupole moment in equation (26), we obtain

$$G_{\rm E2}(q) = \frac{3\gamma_1}{2y^3q^3}\left[2\gamma_1 yq + (y^2q^2 - 4\gamma_1^2)\arctan\left(\frac{yq}{2\gamma_1}\right)\right]. \tag{29}$$

Note that the result for $G_{\rm E0}(q)$, equation (25), is the same for a spin $1/2$ dimer but appears with the appropriate $J = 3/2$ polarization matrix in equation (23).

### 3.2. Vector current

Next, we investigate the vector electromagnetic current of $^{31}$Ne. For this purpose, we consider the amplitude with an irreducible vertex for an $A_k$ photon with four-momentum $(0, \boldsymbol{q})$ coupling to the $^{30}$Ne-$n$ $P$-wave bound state. The corresponding diagrams are depicted in figure 4. The two diagrams on the right, which are crossed out, can be shown to vanish by parity conservation such that only the two diagrams on the left contribute. Furthermore, we have to take into account local gauge-invariant contributions from the magnetic coupling to the spins of the corresponding fields. Assuming that both the anomalous magnetic moment of the neutron $\kappa_n$ and the magnetic moment of the dimer $L_{\rm M}$ scale naturally, they contribute to LO. As a matter of fact, the counterterm $L_{\rm M}$ is necessary for renormalization purposes already at LO. The diagrams are shown in figure 5 and the corresponding magnetic interaction vertices are given by

$$\mathscr{L}^n_{\rm M} = \kappa_n \mu_N \, n^\dagger_{\alpha'}(2\boldsymbol{S}_{\frac{1}{2}} \cdot \boldsymbol{B})_{\alpha'\alpha} n_\alpha, \tag{30}$$

$$\mathscr{L}^{\pi}_{\mathrm{M}} = L_{\mathrm{M}}\mu_N\ \pi^{\dagger}_{\beta'}\left(\frac{2}{3}\boldsymbol{S}_{\frac{3}{2}}\cdot\boldsymbol{B}\right)_{\beta'\beta}\pi_{\beta}, \tag{31}$$

where $\kappa_n$ denotes the anomalous magnetic moment of the neutron and $\mu_N$ is the nuclear magneton (see [38] for a discussion of the $J^P = 1/2^+$ case). $L_{\mathrm{M}}$ is a counterterm required for renormalization. Furthermore, $\boldsymbol{B} = (\boldsymbol{\nabla}\times\boldsymbol{A})$ is the magnetic field of the photon while $\boldsymbol{S}_J$ is a three-dimensional vector with spin matrices as its components. These matrices depend on the total spin $J$ of the considered field as indicated by the subscript $J$. In our case, $J = 1/2$ for the neutron while $J = 3/2$ for the dimer field. The magnetic operators in equations (30), (31) are written in the form

$$\frac{1}{J}\boldsymbol{S}_J\cdot\boldsymbol{B} = \sum_{m=-1}^{1}\frac{1}{J}(S_J)_m B^m, \tag{32}$$

where $(S_J)_m$ and $B_m$ are the corresponding components in spherical coordinates. The components of the three spin matrices are given by [37]

$$[(S_J))_m]_{\sigma'\sigma} = \sqrt{J(J+1)}\,C^{J\sigma'}_{(J\sigma)(1m)}. \tag{33}$$

Therefore, the matrix element for maximal projection is always multiplied by $B_0$.

The vector electromagnetic transition amplitude can be written as

$$\begin{aligned}\langle\pi_{\beta'}(\boldsymbol{p}')|\ J^k|\pi_{\beta}(\boldsymbol{p})\rangle = &\left[ iq_c eG_{\mathrm{E0}}(q)\sqrt{\frac{4\pi}{1}}\,q^0 Y^*_{00}(\boldsymbol{e_q})(\tilde{T}^{[00]}_{3/2})_{\beta'\beta}\right.\\ &\left.+i\mu_Q G_{\mathrm{E2}}(q)\frac{1}{2}\sqrt{\frac{4\pi}{5}}\,q^2\textstyle\sum_M Y^*_{2M}(\boldsymbol{e_q})(\tilde{T}^{[2M]}_{3/2})_{\beta'\beta}\right]\frac{(\boldsymbol{p}'+\boldsymbol{p})^k}{2M_{nc}}\\ &+i\mu_D G_{\mathrm{M1}}(q)\sqrt{\frac{4\pi}{3}}\,q^1\textstyle\sum_M \sqrt{2}\,C^{1(M+k)}_{(1k)(1M)}Y^*_{1(M+k)}(\boldsymbol{e_q})(\tilde{T}^{[1M]}_{3/2})_{\beta'\beta}\\ &+i\mu_O G_{\mathrm{M3}}(q)\frac{1}{2}\sqrt{\frac{4\pi}{7}}\,q^3\textstyle\sum_M \sqrt{2}\,C^{3(M+k)}_{(1k)(3M)}Y^*_{3(M+k)}(\boldsymbol{e_q})(\tilde{T}^{[3M]}_{3/2})_{\beta'\beta},\end{aligned} \tag{34}$$

where $\mu_D$ denotes the magnetic dipole moment, $\mu_O$ is the magnetic octupole moment, whereas $G_{\mathrm{M1}}$ and $G_{\mathrm{M3}}$ are the corresponding form factors, respectively. As for the scalar current, the multipole moments are explicitly factored out in equation (34) and therefore the form factors are normalized to one in the limit of vanishing photon momentum by construction. Obviously, the physics of the vector electromagnetic current is richer than that of the scalar current. Not only the electric monopole and quadrupole form factor appear in equation (34) but also the magnetic contributions. In our case, or rather for a spin-3/2 particle, in addition to the magnetic dipole moment, there is also a magnetic octupole moment. Due to the integral over the two $P$-wave spherical harmonics and over the spherical harmonic from the vector photon in the second diagram of figure 4, we now have an implicit coupling of three angular momenta. The corresponding photon multipolarities are $L = 0, 1, 2, 3$. However, parity conservation restricts the possible values for the magnetic contributions to $L \in \{1, 3\}$. The contributions of $L = 1$ and $L = 3$ manifest in equation (34) through terms proportional to $Y^*_{1(M+k)}$ and $Y^*_{3(M+k)}$, respectively. In contrast, the electric contributions to the vector current are apparent through the term proportional to $(\boldsymbol{p}'+\boldsymbol{p})^k$.

A closer look at the vector current in equation (34) suggests a generalized structure including arbitrary high multipole electric and magnetic form factors that can be found in appendix C.

The LO results for the magnetic form factors for a $J = 3/2$ dimer read

$$\mu_D G_{\mathrm{M1}}(q) = \left[ a L_{\mathrm{M}}(\mu) + b\kappa_n + c\frac{yq_c}{A_c} \right] \frac{\mu_N}{r_1}, \tag{35}$$

$$\mu_O G_{\mathrm{M3}}(q) = \frac{-\sqrt{6}\,\kappa_n \mu_N}{10 r_1 (1-y) q^3} \left[ 2\gamma_1 (1-y) q + ((1-y)^2 q^2 - 4\gamma_1^2) \arctan\left( \frac{(1-y)q}{2\gamma_1} \right) \right], \tag{36}$$

with $A_c$ denoting the mass number of the core while $a$, $b$ and $c$ are functions given by

$$a = [r_1 + 3(\mu - \gamma_1)], \tag{37}$$

$$b = \frac{1}{(1-y)q} \left[ \frac{21}{10}\gamma_1 (1-y) q + \left( \frac{21}{20}(1-y)^2 q^2 + \frac{9}{5}\gamma_1^2 \right) \arctan\left( \frac{(1-y)q}{2\gamma_1} \right) \right] - 3\mu, \tag{38}$$

$$c = \frac{3}{4q} \left[ 2\gamma_1 q + \frac{(4\gamma_1^2 + y^2 q^2)}{y} \arctan\left( \frac{yq}{2\gamma_1} \right) \right] - 3\mu. \tag{39}$$

For a $J = 1/2$ dimer, only the magnetic dipole form factor is observable. The corresponding functions $a$, $b$ and $c$ slightly differ from the ones given in equations (37), (38) and (39) and can be found in appendix B. The first term in the numerator of equation (35) proportional to $L_{\mathrm{M}}(\mu)$ is a contribution due to the direct magnetic moment coupling to the spin of the dimer field. The second term is a contribution due to the magnetic moment of the neutron proportional to $\kappa_n$. Finally, the origin of the third contribution proportional to $yq_c/A_c$ lies in the finite angular momentum of the charged core which induces a magnetic dipole moment and therefore contributes to the magnetic dipole form factor.

Applying the normalization conditions at the real photon point, $\lim_{q\to 0} G_{\mathrm{M1}}(q) = 1$ and $\lim_{q\to 0} G_{\mathrm{M3}}(q) = 1$, the magnetic dipole and octupole moments are read off as

$$\mu_D = \left[ L_{\mathrm{M}}(\mu) + \frac{3(\mu - \gamma_1)}{r_1} \left( L_{\mathrm{M}}(\mu) - \kappa_n - \frac{yq_c}{A_c} \right) \right] \mu_N, \tag{40}$$

$$\mu_O = -\frac{\sqrt{6}\,(1-y)^2 \kappa_n \mu_N}{15\gamma_1 r_1}. \tag{41}$$

Note that the magnetic dipole moment cannot be predicted in Halo EFT. Instead, the counterterm $L_{\mathrm{M}}(\mu)$ is matched to the magnetic dipole moment using equation (40). The contribution of the dimer to the magnetic moment, $L_{\mathrm{M}}(\mu)$, thus is resolution-dependent. Its scale dependence is governed by the renormalization group equation

$$\mu \frac{\mathrm{d}}{\mathrm{d}\mu} L_{\mathrm{M}}(\mu) = \frac{\mu}{\mu - \gamma_1 + r_1/3} \left[ \kappa_n + \frac{yq_c}{A_c} - L_{\mathrm{M}}(\mu) \right]. \tag{42}$$

However, the full $q^2$-dependence of the product $\mu_D G_{\mathrm{M1}}(q)$ in the transition amplitude, equation (34) is given by Halo EFT. Moreover, the octupole moment, in contrast to the dipole moment, is also predicted by Halo EFT. Inserting equations (41) in (36) yields

$$G_{\mathrm{M3}}(q) = \frac{3\gamma_1}{2(1-y)^3 q^3}\left[2\gamma_1(1-y)q + ((1-y)^2q^2 - 4\gamma_1^2)\arctan\left(\frac{(1-y)q}{2\gamma_1}\right)\right]$$
$$= G_{\mathrm{E2}}(q)[y \to (1-y)]. \tag{43}$$

This is the exact same expression as in equation (29) except for the substitution $y \to (1-y)$ in the dependence on the mass factor from equation (27).

## 4. Bound state observables and their correlations

The electromagnetic form factors from the previous section can be expanded for low three-momentum transfer $q^2$ in order to extract the corresponding radii:

$$G_{(\mathrm{E/M})L}(q) = 1 - \frac{1}{6}\langle r^2_{(\mathrm{E/M})L}\rangle q^2 + ..., \tag{44}$$

where $\langle r^2_{(\mathrm{E/M})L}\rangle$ denotes the expectation value of the electric/magnetic radius squared with multipolarity $L$, respectively. Below, we give general expressions for a halo nucleus with a $J^P = 0^+$ core and a halo neutron in a $J^P = 3/2^-$ $P$-wave state as well as explicit numbers for $^{31}$Ne based on the assumptions discussed in section 2.

### 4.1. Results in the electric sector

The electric monopole and quadrupole radii at LO are

$$\langle r^2_{\mathrm{E0}}\rangle = -\frac{5y^2}{2\gamma_1 r_1}(\text{see also [26]}), \tag{45}$$

$$\langle r^2_{\mathrm{E2}}\rangle = \frac{3y^2}{5\gamma_1^2}. \tag{46}$$

Given these expressions, we can establish universal correlations with other observables. Considering the result for the quadrupole moment in equation (28), we find the correlation

$$\mu_Q = \frac{2}{15}q_c\langle r^2_{\mathrm{E0}}\rangle, \tag{47}$$

which is depicted in the left panel of figure 6. The red solid line indicates our result for $^{31}$Ne for $r_1$ within the estimated interval of $[-150, -50]$ MeV. We obtain

$$\sqrt{\langle r^2_{\mathrm{E0}}\rangle} \in [0.20(08), 0.35(14)]\,\mathrm{fm}, \tag{48}$$

$$\mu_Q \in [0.06(02), 0.17(07)]\,\mathrm{fm}^2, \tag{49}$$

Furthermore, we find a correlation between the quadrupole radius squared $\langle r^2_{\mathrm{E2}}\rangle$ and the neutron separation energy $S_n$ given by

$$\langle r^2_{\mathrm{E2}}\rangle = \frac{3y^2}{10m_R}\frac{1}{S_n}. \tag{50}$$

It is depicted in the right panel of figure 6, where the red cross indicates our $^{31}$Ne result for $S_n = 0.15$ MeV given by

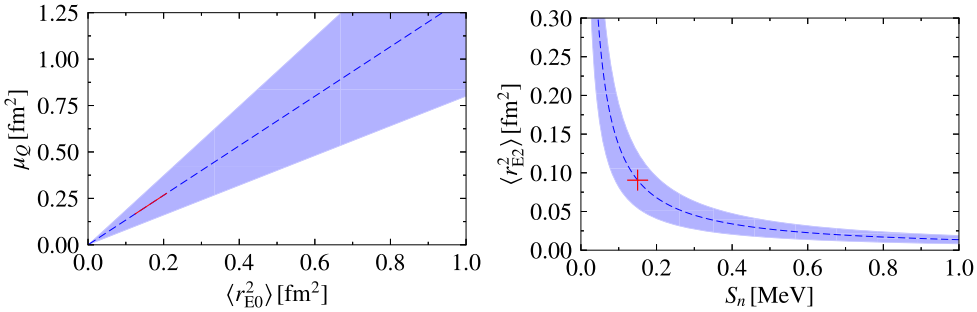


**Figure 6.** Left panel: correlation between the quadrupole moment and the squared charge radius (dashed line). The red solid line indicates our results in case of $r_1$ within the estimated interval of $[-150, -50]$ MeV. Right panel: correlation between the squared quadrupole radius and the neutron separation energy (dashed line). The red cross indicates our result for $S_n = 0.15$ MeV. The blue-shaded bands give our estimate of the EFT uncertainty.

$$\sqrt{\langle r^2_{E2}\rangle} = 0.30(12) \text{ fm}. \tag{51}$$

### *4.2. Results in the magnetic sector*

The LO result for the magnetic octupole radius squared reads

$$\langle r^2_{M3}\rangle = \frac{3(1-y)^2}{5\gamma_1^2} = \frac{3(1-y)^2}{10\mu}\frac{1}{S_n}. \tag{52}$$

This correlation between the squared octupole radius and the neutron separation energy is similar to the correlation in equation (50). The corresponding value for the octupole radius of $^{31}$Ne is

$$\sqrt{\langle r^2_{M3}\rangle} = 9.0(3.6) \text{ fm}. \tag{53}$$

Given the octupole moment in equation (41) and estimating $r_1$ as before yields the following result for the octupole moment of $^{31}$Ne

$$\mu_O \in [-14(6), -5(2)]\,\mu_N \text{fm}^2. \tag{54}$$

Since the magnetic dipole moment contains the counterterm proportional to $L_M(\mu)$, it is not possible to predict its value in Halo EFT. However, as discussed above, the full $q^2$-dependence of $\mu_D G_{M1}(q)$ is predicted. In particular, the 'renormalized magnetic radius' defined as $\mu_D\langle r^2_{M1}\rangle$ is independent of $L_M(\mu)$. For a $J = 3/2$ state, we have

$$\mu_D\langle r^2_{M1}\rangle = -\frac{\mu_N}{\gamma_1 r_1}\left(\frac{3y^3 q_c}{2A_c} + \frac{27}{10}(1-y)^2\kappa_n\right). \tag{55}$$

Using this relation, it is either possible to predict $\langle r^2_{M1}\rangle$ once the magnetic dipole moment is determined experimentally or vice versa. The corresponding result for $J = 1/2$ can again be found in appendix B.

### *4.3. Nuclear deformation*

The appearance of higher multipole moments such as the electric quadrupole as well as the magnetic octupole moment indicates that $^{31}$Ne is not a spherically symmetric nucleus. Following [39], we assume a quadrupolar deformed shape with a sharp edge at radius

$$R_{\rm def} = R_0(1 + \beta_2 Y_{20}(\theta, \phi))/N, \tag{56}$$

where $R_0$ is the equilibrium radius, meaning the radius of the nucleus would be spherically symmetric. The additional term $\beta_2 Y_{20}(\theta, \phi)$ accounts for the quadrupolar deformation where $\beta_2$ is called the deformation parameter. Having defined this surface radius and using $\beta_2 \ll 1$, we can relate it to the spectroscopic quadrupole moment via [39, 40]

$$\begin{aligned}\mu_Q(3/2) &= \frac{1}{5}\sqrt{\frac{16\pi}{5}}\,\frac{3}{4\pi} Ze R_0^2 \beta_2 \\ &= \sqrt{\frac{1}{5\pi}}\, Ze\beta_2 \langle r_{\rm E0}^2 \rangle. \end{aligned} \tag{57}$$

In the second line of equation (57) we used $\langle r_{\rm E0}^2 \rangle = (3/5)R_0^2$. As a result, we find a linear correlation between the quadrupole moment and the mean squared electric monopole radius. This is exactly the same correlation we found in our Halo EFT calculation and hence equating the proportionality factors allows us to determine the deformation parameter of $^{31}$Ne to be $\beta_2 = 0.53$. This value is similar to $\beta_2 = 0.41$ found in an antisymmetrized molecular dynamics calculation with the Gogny D1S interaction [22]. A deformation parameter of $\beta_2 \approx 0.4$ was also obtained in [23] from the analysis of parallel momentum distribution of the charged fragment in the breakup of $^{31}$Ne. These values indicate a significant deformation due to the non-vanishing quadrupole moment. However, we note that our prediction is solely determined by the dynamics of the electrically charged core. The deformation of the core itself is not included here. In this sense, our predictions are relative to the core. Once the intrinsic properties of the core are experimentally determined, they can be included in our theory. In particular, intrinsic deformation properties of the core such as its quadrupole moment due to the $J^P = 2^+$ excited state can be described explicitly in Halo EFT by including a corresponding field in the effective Lagrangian. This would allow us to predict the deformation properties due to both the intrinsic core properties and the dynamics of the halo nucleus. Indeed, it is expected to find a quadrupolar deformation of the $^{30}$Ne core. Urata *et al* [21] showed that the deformation parameter of the $^{30}$Ne core is around $\beta_2 = 0.2...0.3$, while Minomo *et al* [22] found $\beta_2 = 0.39$. Therefore, the total quadrupolar deformation of $^{31}$Ne is ultimately composed of both deformation effects.

## 5. E1 breakup: $^{31}$Ne into $^{30}$Ne and a neutron

In figure 7, we show the LO diagram contributing to the E1 breakup of $^{31}$Ne. The photon transfers an angular momentum of 1 on to the two-body system consisting of the core and neutron. Since this two-body system is bound in a *P*-wave, the possible final angular momenta in the continuum are 0 and 2, corresponding to an *S*- and a *D*-wave, respectively.

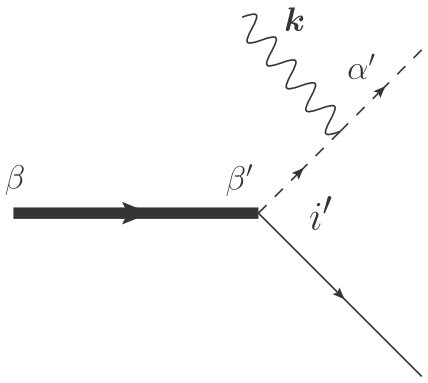


**Figure 7.** E1 breakup of $^{31}$Ne into the continuum consisting of the core and neutron. We use the same notation as in figure 2.

The scalar transition amplitude in momentum space is given by

$$\Gamma_0^{\alpha'\beta} = \frac{i2m_R g_1 q_c e\sqrt{Z_\pi} C^{\frac{3}{2}\beta}_{(1i')(\frac{1}{2}\alpha')}(\boldsymbol{p} - y\boldsymbol{k})_{i'}}{\gamma_1^2 + (\boldsymbol{p} - y\boldsymbol{k})^2}, \tag{58}$$

$$= iq_c e\langle \boldsymbol{p} - y\boldsymbol{k}|\psi^{\alpha'\beta}\rangle, \tag{59}$$

where $|\psi^{\alpha'\beta}\rangle$ represents the bound state of $^{31}$Ne (see appendix D for explicit expressions), the mass ratio $y$ is defined in equation (27), $\boldsymbol{p}$ is the relative momentum between the core and the neutron, while $\boldsymbol{k}$ is the photon momentum.

Without loss of generality, we choose the photon to be traveling in the $\hat{z}$-direction. We insert in equation (59) an identity operator in configuration space and express $e^{iykz}$ by its plane wave expansion

$$e^{iykz} = e^{iykr\cos\theta} = \sqrt{4\pi}\sum_L \sqrt{2L+1}\, i^L j_L(ykr) Y_{L0}(\boldsymbol{e_r}), \tag{60}$$

where $j_L(x)$ is a spherical Bessel function. In the low-energy limit, we use $j_L(ykr) \approx (ykr)^L/(2L+1)!!$.

The scalar transition amplitude then reads

$$\Gamma_0^{\alpha'\beta} = i\sum_L \int \mathrm{d}^3 r \langle \boldsymbol{p}|\ \hat{\tilde{\rho}}_L(\boldsymbol{r})|\psi^{\alpha'\beta}\rangle \sqrt{4\pi}\sqrt{2L+1}\, i^L \frac{(kr)^L}{(2L+1)!!} Y_{L0}(\boldsymbol{e_r}), \tag{61}$$

where

$$\hat{\tilde{\rho}}_L(\boldsymbol{r}) = eZ_{\mathrm{eff}}^{(L)}|\boldsymbol{r}\rangle\langle\boldsymbol{r}| \tag{62}$$

with $Z_{\mathrm{eff}}^{(L)} = q_c y^L$.

This means, that the photon in figure 7 transfers all possible angular momenta. For a specific angular momentum transfer, the amplitude reads

$$\Gamma_0^{\alpha'\beta}(\mathrm{EL};\, M=0) = i\int \mathrm{d}^3 r \langle \boldsymbol{p}|\ \hat{\tilde{\rho}}_L(\boldsymbol{r})|\psi^{\alpha'\beta}\rangle \sqrt{4\pi}\sqrt{2L+1}\, i^L \frac{(kr)^L}{(2L+1)!!} Y_{L0}(\boldsymbol{e_r}). \tag{63}$$

The matrix element relevant for the calculation of the EL breakup is given by [41]

$$\mathscr{M}(\mathrm{EL};\, 0) = \int \mathrm{d}^3 r \langle \boldsymbol{p}|\ \hat{\tilde{\rho}}_L(\boldsymbol{r})|\psi^{\alpha'\beta}\rangle r^L Y_{L0}(\boldsymbol{e_r}), \tag{64}$$

$$= -i\frac{(2L+1)!!}{k^L}(i)^{-L}\sqrt{\frac{1}{4\pi(2L+1)}}\,\Gamma_0^{\alpha'\beta}(\mathrm{EL};\,0). \tag{65}$$

Since we are interested in the E1 breakup, we set $L=1$ in equation (65). Moreover, we plug in the bound state wave function in configuration space given by

$$\begin{aligned}\langle \boldsymbol{r}|\psi^{\alpha'\beta}\rangle &= i\sqrt{\frac{-2\gamma_1^2}{r_1}}\,\frac{e^{-\gamma_1 r}}{r}\left(1+\frac{1}{\gamma_1 r}\right)Y_{1i'}(\boldsymbol{e_r})\,C^{\frac{3}{2}\beta}_{(1i')(\frac{1}{2}\alpha')}\\ &= i\;C_\pi\frac{u(r)}{r}Y_{1i'}(\boldsymbol{e_r})\,C^{\frac{3}{2}\beta}_{(1i')(\frac{1}{2}\alpha')},\end{aligned} \tag{66}$$

with $C_\pi$ denoting the asymptotic normalization constant (ANC) and $u(r)$ the radial wave function. They read

$$C_\pi = \sqrt{\frac{-2\gamma_1^2}{r_1}}, \tag{67}$$

$$u(r) = e^{-\gamma_1 r}\left(1+\frac{1}{\gamma_1 r}\right). \tag{68}$$

This yields

$$\mathscr{M}(\mathrm{E1};\,0) = ieZ^{(1)}_{\mathrm{eff}}C_\pi\int \mathrm{d}^3 r e^{-i\boldsymbol{pr}}u(r)\,Y_{1i'}(\boldsymbol{e_r})\,Y_{10}(\boldsymbol{e_r})\,C^{\frac{3}{2}\beta}_{(1i')(\frac{1}{2}\alpha')}. \tag{69}$$

The product of the spherical harmonics in equation (69) can be expressed as an irreducible sum of spherical harmonics with $L=0$ and $L=2$. This allows us to extract the two relevant matrix elements for a transition into either an $S$-wave or a $D$-wave.

The $P\to S$ transition amplitude reads

$$\mathscr{M}(\mathrm{E1};\,0;\,P\to S) = \frac{ieZ^{(1)}_{\mathrm{eff}}C_\pi}{\sqrt{4\pi}}\int \mathrm{d}^3 r e^{-i\boldsymbol{pr}}u(r)\,Y_{00}(\boldsymbol{e_r})\,C^{\frac{3}{2}\beta}_{(10)(\frac{1}{2}\alpha')}. \tag{70}$$

We use the plane wave expansion of $e^{-i\boldsymbol{pr}}$, integrate over $d\Omega$ and couple the angular momentum of $L=0$ and the spin of the neutron to a two-particle continuum with total spin quantum numbers $(J'\beta')$ to find

$$\mathscr{M}^{J'\beta'\beta}(\mathrm{E1};\,0;\,P\to S) = ieZ^{(1)}_{\mathrm{eff}}C_\pi\sqrt{4\pi}\,Y_{00}(\boldsymbol{e_p})\int \mathrm{d}r j_0(pr)u(r)r^2 C^{\frac{3}{2}\beta}_{(10)(\frac{1}{2}\alpha')}\,C^{J'\beta'}_{(00)(\frac{1}{2}\alpha')}. \tag{71}$$

We proceed similarly for the $P\to D$ transition amplitude and find

$$\begin{aligned}\mathscr{M}^{J'\beta'\beta}(\mathrm{E1};\,0;\,P\to D) &= -ieZ^{(1)}_{\mathrm{eff}}C_\pi\sqrt{\frac{24\pi}{5}}\sum_m Y_{2m}(\boldsymbol{e_p})\\ &\times\int \mathrm{d}r j_2(pr)u(r)r^2 C^{2m}_{(1i')(10)}\,C^{\frac{3}{2}\beta}_{(1i')(\frac{1}{2}\alpha')}\,C^{J'\beta'}_{(2m)(\frac{1}{2}\alpha')}.\end{aligned} \tag{72}$$

Performing the radial integral and sum (average) over final (initial) spins and multiply our results with a factor of 3 to make up for the fact that we chose the photon to propagate in the $\hat{z}$-direction, we finally get

$$\overline{|\mathscr{M}(\mathrm{E1};\,P\to S)|}^2 = e^2 Z^{(1)2}_{\mathrm{eff}}\,|C_\pi|^2 4\pi\,|Y_{00}(\boldsymbol{e_p})|^2\frac{(3\gamma_1^2+p^2)^2}{\gamma_1^2(\gamma_1^2+p^2)^4}, \tag{73}$$

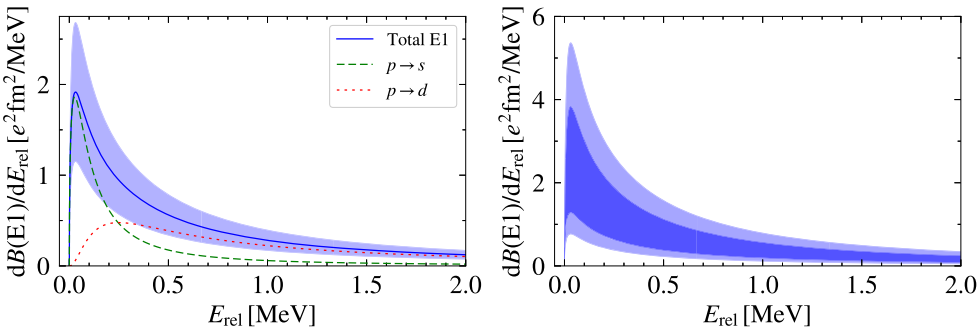


**Figure 8.** Differential E1 transition strength of $^{31}$Ne as a function of the relative energy $E_{\rm rel}$ of the $^{30}$Ne core and the neutron. Left panel: separate contributions shown for $r_1 = -100$ MeV. An explanation of curves is given in inset. Right panel: dark shaded band gives the uncertainty from $r_1$ estimated as $r_1 \in [-150, -50]$ MeV, while the light-shaded bands also include the general EFT uncertainty at LO of 40%.

$$\overline{|\mathscr{M}(\mathrm{E1};\, P \to D)|}^2 = e^2 Z_{\rm eff}^{(1)2}\, |C_\pi|^2 \frac{24\pi}{5} \sum_m |Y_{2m}(\boldsymbol{e}_{\boldsymbol{p}})|^2 \frac{4p^4}{\gamma_1^2(\gamma_1^2 + p^2)^4} \sum_{i'} (C^{2m}_{(1i')(10)})^2. \tag{74}$$

The differential E1 transition strength is given by [42]

$$\mathrm{dB(E1)} = \overline{|\mathscr{M}(\mathrm{E1})|}^2 \frac{\mathrm{d}^3 p}{(2\pi)^3}. \tag{75}$$

Using $E_{\rm rel} = p^2/(2m_R)$, the differential E1 transition strength as a function of the relative energy $E_{\rm rel}$ between the core and neutron reads

$$\frac{\mathrm{dB(E1)}}{\mathrm{d}E_{\rm rel}} = \frac{1}{(2\pi)^3} \int \mathrm{d}\Omega_{\boldsymbol{p}} m_R\, p\, \overline{|\mathscr{M}(\mathrm{E1})|}^2. \tag{76}$$

The final results for both transitions read

$$\frac{\mathrm{dB(E1};\, P \to S)}{e^2 \mathrm{d}E_{\rm rel}} = Z_{\rm eff}^{(1)2} \frac{m_R}{2\pi^2}\, |C_\pi|^2 \frac{p}{\gamma_1^2} \frac{(3\gamma_1^2 + p^2)^2}{(\gamma_1^2 + p^2)^4}, \tag{77}$$

$$\frac{\mathrm{dB(E1};\, P \to D)}{e^2 \mathrm{d}E_{\rm rel}} = Z_{\rm eff}^{(1)2} \frac{m_R}{\pi^2}\, |C_\pi|^2 \frac{p}{\gamma_1^2} \frac{4p^4}{(\gamma_1^2 + p^2)^4}. \tag{78}$$

In the left panel of figure 8, we show the corresponding curves for a $P$-wave effective momentum $r_1 = -100$ MeV. As expected, the $S$-wave contribution in the continuum dominates at low energies while the $D$-wave contribution takes over around $E_{\rm rel} = 0.25$ MeV. The total differential B(E1) transition strength is given in blue while the blue-shaded band represents a 40% estimate of the EFT uncertainty at LO from our power counting. In the right panel of figure 8, the dark shaded band gives the uncertainty of the total differential B(E1) transition strength from $r_1$ estimated as $r_1 \in [-150, -50]$ MeV, while the light-shaded bands also include the general EFT uncertainty at LO of 40%.

The bare cross section corresponding to an infinite energy resolution of the detector is given by [43, 44]

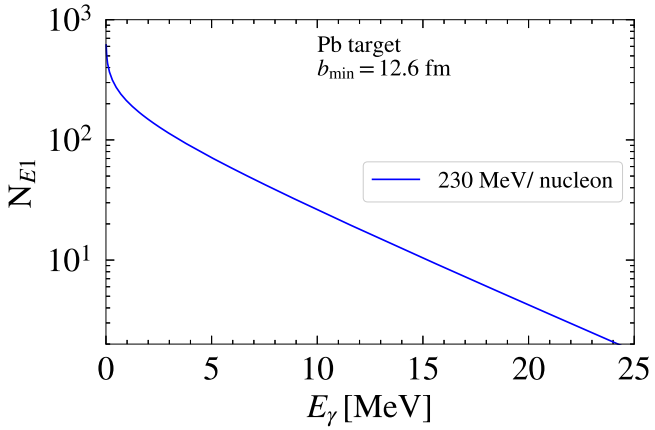


**Figure 9.** Total virtual photon number as a function of the photon energy $E_\gamma$ for a lead target at impact parameters $b_{\min} = 12.6$ fm and larger (i.e. integrated over impact parameters) and a kinetic energy of 230 MeV per nucleon [16] calculated using equation (80).

$$\frac{\mathrm{d}\sigma}{\mathrm{d}E_{\mathrm{rel}}}(E_{\mathrm{rel}}) = \frac{16\pi^3}{9}\alpha N_{\mathrm{E1}}(E_\gamma, b_{\min})\frac{\mathrm{dB(E1)}}{e^2\mathrm{d}E_{\mathrm{rel}}}, \tag{79}$$

where $E_{\mathrm{rel}} = E_\gamma - S_n + k^2/(2M_{nc})$ with $S_n$ the neutron separation energy of $^{31}$Ne. The expression for the virtual photon flux $N_{\mathrm{E1}}(E_\gamma, b_{\min})$ integrated overall impact parameters larger than $b_{\min}$ is given by [43]

$$N_{\mathrm{E1}}(E_\gamma, b_{\min}) = \frac{2Z_t^2\alpha}{\pi\beta^2}\left(\xi K_0(\xi)K_1(\xi) - \frac{\beta^2\xi^2}{2}(K_1^2(\xi) - K_0^2(\xi))\right), \tag{80}$$

where $Z_t$ is the charge of the target, $\xi = E_\gamma b_{\min}/(\gamma\beta)$ with $\gamma = (1-\beta^2)^{-1/2}$ the Lorentz factor of the beam. The corresponding plot can be found in figure 9. We note that equation (79) holds in natural units with $\hbar = c = 1$ for either the Heaviside–Lorentz convention or any other CGS system of units (see also [45]). Since no experimental results have been published to date, we have folded the predicted bare cross section with a hypothetical Gaussian energy resolution

$$g(E) = \frac{1}{\sqrt{2\pi}\,\sigma(E)}e^{-\frac{1}{2}(E/\sigma(E))^2}, \tag{81}$$

with an energy-dependent width $\sigma(E) = (0.15\sqrt{\mathrm{MeV}})\sqrt{E}$ to allow for a more realistic comparison to future experimental data. The resolution averaged cross section is obtained from

$$\left\langle \frac{\mathrm{d}\sigma}{\mathrm{d}E_{\mathrm{rel}}}(E_{\mathrm{rel}}) \right\rangle = \int dE'\, \frac{\mathrm{d}\sigma}{\mathrm{d}E'}(E')g(E_{\mathrm{rel}} - E'), \tag{82}$$

and shown in figure 10 for a $P$-wave effective momentum $r_1 = -100$ MeV. The total differential cross section for E1 breakup of $^{31}$Ne is given in blue while the blue-shaded band represents a 40% estimate of the EFT uncertainty at LO from our power counting. We note that in any experiment there is also a contribution from a nuclear breakup. An estimate of the error from the nuclear contribution is beyond the scope of this work. We refer the reader to the discussion in [14, 46] in the case of $^{11}$Be. The absolute height of the peak has a large EFT

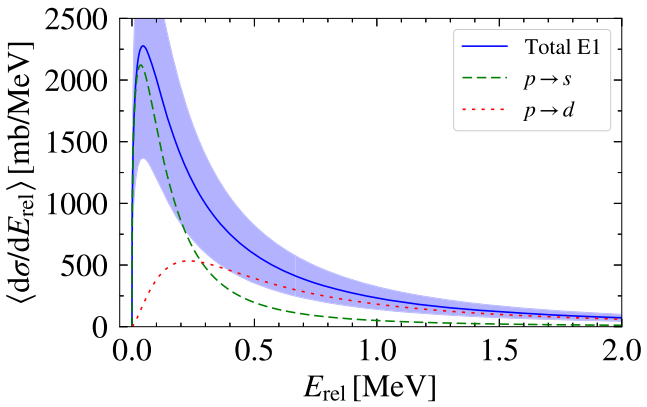


**Figure 10.** Differential cross section for E1 breakup of $^{31}$Ne folded with a Gaussian energy resolution of width $\sigma(E) = (0.15\sqrt{\text{MeV}})\sqrt{E}$ as a function of the relative energy $E_{\text{rel}}$ of the $^{30}$Ne core and the neutron for $r_1 = -100$ MeV. The light-shaded band gives the EFT uncertainty at LO of 40%. An explanation of curves is given in inset.

uncertainty while the shape of the curve is rather robust. However, it is strongly influenced by the assumed detector resolution parameter $\sigma$ and larger values of $\sigma$ will further smear the peak. We note that for the sake of clarity the results for the E1 breakup of $^{31}$Ne are shown for the fixed neutron separation energy $B_1 = 150$ keV given by the central value in [17]. In general, the results depend on the neutron separation energy. A hypothetical higher (lower) separation energy would lead to a decreased (increased) absolute peak height as well as a shift of the peak position to higher (lower) relative energies.

## 6. Conclusion

We have investigated the electromagnetic properties of $^{31}$Ne using Halo EFT. Instead of using standard Cartesian coordinates, we have introduced a spherical basis that is ideally suited for the description of halo nuclei beyond the *S*-wave. It uses the correct number of degrees of freedom by construction and therefore leads to more compact and simplified expressions. We expect it to be useful in future studies of halo nuclei with higher angular momentum.

In our study of the electric properties, we found that our numerical predictions are fairly small. We calculated the charge radius as $\langle r_{\text{E0}}^2\rangle^{1/2} \in [0.20(08), 0.35(14)]$ fm and the quadrupole moment as $\mu_Q \in [0.06(02), 0.17(07)]$ fm$^2$, where the numbers in square brackets give the results for $r_1 = -150$ MeV and $-50$ MeV, respectively, while the number in parentheses indicates the error from higher orders in the EFT expansion. The corresponding quadrupole radius is independent of $r_1$ and predicted to be $\langle r_{\text{E2}}^2\rangle^{1/2} = 0.30(12)$ fm.

These values are rather small because at leading order they are solely determined by the motion of the electrically charged core around the center-of-mass. Since the $^{30}$Ne core is almost as heavy as the total system, $^{31}$Ne, this yields small predictions. Therefore, we expect the internal electric properties of the core to be important, at least in the electric sector. Such effects can be included at NLO by treating excited states of the core as explicit fields or via counterterms. See [47] for a discussion of this issue in the case of the charge radius.

Once more experimental data is available, the treatment of the first excited state of the $^{30}$Ne core as an explicit degree of freedom within Halo EFT becomes feasible. This would lead to

more precise predictions in the electric sector and potentially to a smaller expansion parameter. Alternatively, one could include the excited states of the core by describing the halo nucleus as a neutron coupled to a rotor similar to the work of [48, 49].

Nevertheless, in the magnetic sector the main contribution to observables arises from the motion of the valence neutron around the center-of-mass. This means that corrections due to the internal core properties at NLO should be negligible. As a matter of fact, in the magnetic case our numerical predictions are much larger, $\langle r_{\mathrm{M3}}^2\rangle^{1/2} = 9.0(3.6)$ fm and $\mu_O \in [-14(6), -5(2)]\,\mu_N\,\mathrm{fm}^2$. The large octupole radius reveals the size of the halo system. Unfortunately, the magnetic dipole moment cannot be predicted since it depends on the counterterm $L_{\mathrm{M}}$ already at LO.

In general, the non-vanishing higher multipole moments with multipolarity $L > 1$ indicate that $^{31}$Ne is not a spherically symmetric nucleus. We extracted the $\beta_2$-deformation parameter from the linear correlation between the quadrupole moment and the charge radius and found $\beta_2 = 0.53$. This value indicates a significant deformation due to the quadrupole moment. However, we note that this prediction is solely determined by the dynamics of the electrically charged core whereas the deformation of the core itself is not included here. In this sense, our prediction is relative to the core. Intrinsic deformation properties of the core can be described explicitly in Halo EFT by introducing corresponding fields in the effective Lagrangian. Once more experimental data of the intrinsic deformation properties of the core such as its quadrupole moment are available, they can be included in Halo EFT to calculate the total deformation properties due to both the intrinsic core properties and the dynamics of the halo nucleus.

Moreover, we have derived the differential B(E1) transition strength as a function of the relative energy $E_{\mathrm{rel}}$ between the $^{30}$Ne core and the neutron. This transition strength together with the virtual photon number allowed us to calculate the differential cross section for E1 breakup of $^{31}$Ne. In order to take into account a realistic limited energy resolution in experiment, we have folded our results with a Gaussian energy resolution of width 0.1 MeV. Comparing these results to future data will help us to further determine unknown parameters which in turn enables us to improve our Halo EFT for $^{31}$Ne. Finally, an application of our formalism to $^{37}$Mg [18], which is also a candidate for a deformed $P$-wave halo nucleus appears promising.

## Acknowledgments

This work was supported by the Deutsche Forschungsgemeinschaft (DFG, German Research Foundation)—Project number 279384907—CRC 1245 and by the German Federal Ministry of Education and Research (BMBF) (Grant No. 05P21RDFNB).

## Data availability statement

The data that support the findings of this study are available upon reasonable request from the authors.

## Appendix A. Spherical coordinates

Throughout this work, we use spherical coordinates. The components of a three-dimensional vector are written as

$$r_i = \sqrt{\frac{4\pi}{3}}\, rY_{1i}(\boldsymbol{e_r}), \tag{A1}$$

$$r^i = \sqrt{\frac{4\pi}{3}}\, rY^*_{1i}(\boldsymbol{e_r}), \tag{A2}$$

with the connection to Cartesian coordinates given by

$$r_1 = (r^1)^* = \sqrt{\frac{4\pi}{3}}\, rY_{11} = \sqrt{\frac{4\pi}{3}}\, r\left(-\sqrt{\frac{3}{8\pi}}\right)\sin(\theta)e^{i\phi} = -\frac{r_x + ir_y}{\sqrt{2}}, \tag{A3}$$

$$r_0 = (r^0)^* = \sqrt{\frac{4\pi}{3}}\, rY_{10} = \sqrt{\frac{4\pi}{3}}\, r\sqrt{\frac{3}{4\pi}}\,\cos(\theta) = r_z, \tag{A4}$$

$$r_{-1} = (r^{-1})^* = \sqrt{\frac{4\pi}{3}}\, rY_{1-1} = \sqrt{\frac{4\pi}{3}}\, r\sqrt{\frac{3}{8\pi}}\,\sin(\theta)e^{-i\phi} = \frac{r_x - ir_y}{\sqrt{2}}. \tag{A5}$$

The components of the nabla operator in spherical coordinates expressed in terms of the Cartesian components are given by

$$\nabla_1 = -\frac{1}{\sqrt{2}}\left(\frac{\partial}{\partial x} + i\frac{\partial}{\partial y}\right), \tag{A6}$$

$$\nabla_0 = \frac{\partial}{\partial z}, \tag{A7}$$

$$\nabla_{-1} = \frac{1}{\sqrt{2}}\left(\frac{\partial}{\partial x} - i\frac{\partial}{\partial y}\right). \tag{A8}$$

## Appendix B. $J = 1/2$ case

The on-shell neutron-core scattering amplitude for a $P$-wave with $J = 1/2$ in the center-of-mass frame with $E = p^2/(2m_R) = p'^2/(2m_R)$ and $p = |\boldsymbol{p}| = |\boldsymbol{p}'|$ reads

$$T_{\alpha'\alpha}(\boldsymbol{p}', \boldsymbol{p}) = \frac{6\pi}{m_R}\,\frac{\frac{1}{3}\,\boldsymbol{p}'\cdot\boldsymbol{p}\;\delta_{\alpha'\alpha} + \frac{i}{3}(\boldsymbol{\sigma}\cdot(\boldsymbol{p}'\times\boldsymbol{p}))_{\alpha'\alpha}}{\left(\frac{6\pi\Delta_1}{m_R g_1^2} + \frac{3\pi\eta_1}{m_R^2 g_1^2}p^2 + \frac{3}{2}\mu p^2 + ip^3\right)}, \tag{B1}$$

where $\boldsymbol{\sigma}$ is the three-dimensional vector with the Pauli matrices as its components.

The corresponding LO result for the magnetic dipole form factor for a $J = 1/2$ dimer is

$$G_{\mathrm{M1}}(q) = \frac{1}{r_1}\left[\frac{aL_{\mathrm{M}}^{1/2}(\mu) + b\kappa_n + c\frac{yq_c}{A_c}}{\mu_D}\right]\mu_N, \tag{B2}$$

with $A_c$ denoting the mass number of the core, while $a$, $b$ and $c$ are functions given by

$$a = [r_1 + 3(\mu - \gamma_1)], \tag{B3}$$

$$b = \mu - \gamma_1 - \frac{(1-y)q}{2}\arctan\left(\frac{(1-y)q}{2\gamma_1}\right), \tag{B4}$$

$$c = \frac{1}{2q}\left[2\gamma_1 q + \frac{(4\gamma_1^2 + y^2q^2)}{y}\arctan\left(\frac{yq}{2\gamma_1}\right)\right] - 2\mu, \tag{B5}$$

where the definition of the mass ratio $y$ is given in equation (27). The dipole moment of a $J = 1/2$ dimer also depends on an unknown counterterm $L_{\rm M}^{1/2}(\mu)$ and is given by

$$\mu_D = \left[L_{\rm M}^{1/2}(\mu) + \frac{(\mu - \gamma_1)}{r_1}\left(3L_{\rm M}(\mu) + \kappa_n - 2\frac{yq_c}{A_c}\right)\right]\mu_N. \tag{B6}$$

In contrast, the 'renormalized magnetic radius' $\mu_D\langle r_{\rm M1}^2\rangle$ is independent of $L_{\rm M}^{1/2}(\mu)$ and the result for a $J = 1/2$ state reads

$$\mu_D\langle r_{\rm M1}^2\rangle = \frac{\mu_N}{\gamma_1 r_1}\left(\frac{3}{2}(1-y)^2\kappa_n - y^2\frac{yq_c}{A_c}\right). \tag{B7}$$

## Appendix C. Vector current for arbitrary multipolarity

The generalized structure of the vector current for arbitrary multipolarity can be deduced from equation (34). In particular, the electric form factors in the vector current with an even multipolarity $L$ for a particle with total spin $J$ appear as

$$\left(i\mu_{\rm EL}G_{\rm EL}(q)\frac{1}{a(L)}\sqrt{\frac{4\pi}{2L+1}}q^L\sum_M Y^*_{LM}(\boldsymbol{e_q})(\tilde{T}_J^{[LM]})_{\beta'\beta}\right)\frac{(\boldsymbol{p'}+\boldsymbol{p})^k}{2M_{nc}}, \tag{C1}$$

where $a(L)$ denotes the leading denominators of the Legendre polynomials given by

$$a(L) = 2^{\left(\text{Floor}\left[\frac{L}{2}\right]+\text{Floor}\left[\frac{L}{4}\right]+\text{Floor}\left[\frac{L}{8}\right]+\text{Floor}\left[\frac{L}{16}\right]+\ldots\right)}, \tag{C2}$$

while $\mu_{\rm EL}$ stands for the electric multipole moment and Floor $[x]$ gives the greatest integer less than or equal to $x$.

The magnetic form factors in the vector current with an odd multipolarity $L$ for a particle with total spin $J$ appear as

$$i\mu_{\rm ML}G_{\rm ML}(q)\frac{1}{a(L)}\sqrt{\frac{4\pi}{2L+1}}q^L\sum_M \sqrt{2}\,C^{L(M+k)}_{(1k)(LM)}Y^*_{L(M+k)}(\boldsymbol{e_q})(\tilde{T}_J^{[LM]})_{\beta'\beta}, \tag{C3}$$

where $\mu_{\rm ML}$ denotes the magnetic multipole moment.

## Appendix D. *P*-wave halo EFT wave function

In this section, we calculate the wave function for a $P$-wave bound state mentioned in section 5.

For the derivation of the wave function, we use

$$G_{i'i} \sim \frac{|\psi_{i'}><\psi_i|}{E + B_1} \quad \text{for } E \to -B_1, \tag{D1}$$

where $G_{i'i}$ is the fully interacting Green's function, $B_1$ is the binding energy, and $|\psi_i\rangle$ denotes the corresponding $P$-wave bound state.

Furthermore, we use

$$G_{i'i} = G^0\delta_{i'i} + G^0T_{i'i}G^0, \tag{D2}$$

where $G^0$ and $T_{i'i}$ are the free Green's function and the $P$-wave T-matrix, respectively.

Since the free Green's function gives no contribution to the pole, we find from equations (D1) and (D2)

$$\lim_{E\to -B_1}\frac{\langle \boldsymbol{k}'|\psi_{i'}\rangle\langle\psi_i|\boldsymbol{k}\rangle}{E+B_1} = \lim_{E\to -B_1}\langle \boldsymbol{k}'|\ G^0T_{i'i}G^0|\boldsymbol{k}\rangle. \tag{D3}$$

We consider

$$\begin{aligned}\lim_{E\to -B_1}\langle \boldsymbol{k}'|\ G^0T_{i'i}G^0|\boldsymbol{k}\rangle &= \lim_{E\to -B_1}\frac{1}{E-\frac{k'^2}{2m_R}+i\epsilon}\langle \boldsymbol{k}'|T_{i'i}|\boldsymbol{k}\rangle\frac{1}{E-\frac{k^2}{2m_R}+i\epsilon}\\ &=\frac{1}{B_1+\frac{k'^2}{2m_R}}(g_1^2D_1(-B_1)k'_{i'}k_i^*)\frac{1}{B_1+\frac{k^2}{2m_R}},\end{aligned} \tag{D4}$$

where we have used

$$\langle \boldsymbol{k}'|T_{i'i}|\boldsymbol{k}\rangle = g_1^2D_1(E)k'_{i'}k_i^*, \tag{D5}$$

with $D_1(E)$ denoting the full dimer propagator for the $P$-wave bound state.

Making use of the expansion of the full dimer propagator around the bound state energy $B_1$

$$\lim_{E\to -B_1}D_1(E) = \frac{Z_\pi}{E+B_1}, \tag{D6}$$

we obtain

$$\lim_{E\to -B_1}\langle \boldsymbol{k}'|\ G^0T_{i'i}G^0|\boldsymbol{k}\rangle = \lim_{E\to -B_1}\frac{2m_Rg_1\sqrt{Z_\pi}k'_{i'}}{\gamma_1^2+k'^2}\frac{1}{E+B_1}\frac{2m_Rg_1\sqrt{Z_\pi}k_i^*}{\gamma_1^2+k^2}. \tag{D7}$$

Comparing this result to equation (D3) yields the wave function in momentum space

$$\langle \boldsymbol{k}|\psi_i\rangle = \frac{2m_Rg_1\sqrt{Z_\pi}k_i}{\gamma_1^2+k^2}. \tag{D8}$$

Finally, coupling the orbital angular momentum with quantum numbers $(1i)$ with the spin of the neutron with quantum numbers $(\frac{1}{2}\alpha)$ to the total angular momentum $(\frac{3}{2}\beta)$ leads to

$$\langle \boldsymbol{k}|\psi^{\alpha\beta}\rangle = \frac{2m_Rg_1\sqrt{Z_\pi}k_iC^{\frac{3}{2}\beta}_{(1i)(\frac{1}{2}\alpha)}}{\gamma_1^2+k^2}. \tag{D9}$$

## ORCID iDs

Wael Elkamhawy https://orcid.org/0000-0002-7530-2324
Hans-Werner Hammer https://orcid.org/0000-0002-2318-0644

## References

[1] Hansen P G, Jensen A S and Jonson B 1995 *Ann. Rev. Nucl. Part. Sci.* **45** 591
[2] Jonson B 2004 *Phys. Rep.* **389** 1
[3] Riisager K 2013 *Phys. Scr.* T **152** 014001

[4] Tanihata I 2016 *Eur. Phys. J. Plus* **131** 90
[5] Jensen A S, Riisager K, Fedorov D V and Garrido E 2004 *Rev. Mod. Phys.* **76** 215
[6] Braaten E and Hammer H-W 2006 *Phys. Rep.* **428** 259
[7] Hammer H-W, Ji C and Phillips D R 2017 *J. Phys.* G **44** 103002
[8] Bertulani C A, Hammer H-W and Kolck U Van 2002 *Nucl. Phys.* A **712** 37
[9] Bedaque P F, Hammer H-W and van Kolck U 2003 *Phys. Lett.* B **569** 159
[10] Epelbaum E, Hammer H-W and Meissner U-G 2009 *Rev. Mod. Phys.* **81** 1773
[11] Machleidt R and Entem D R 2011 *Phys. Rep.* **503** 1
[12] Hammer H W, König S and van Kolck U 2020 *Rev. Mod. Phys.* **92** 025004
[13] Capel P, Phillips D R and Hammer H W 2018 *Phys. Rev.* C **98** 034610
Capel P, Phillips D R and Hammer H W 2022 *Phys. Rev.* C **105** 019901
[14] Capel P, Phillips D R and Hammer H W 2022 *Phys. Lett.* B **825** 136847
[15] Moro A M and Lay J A 2012 *Phys. Rev. Lett.* **109** 232502
[16] Nakamura T *et al* 2009 *Phys. Rev. Lett.* **103** 262501
[17] Nakamura T *et al* 2014 *Phys. Rev. Lett.* **112** 142501
[18] Kobayashi N *et al* 2014 *Phys. Rev. Lett.* **112** 242501
[19] Zhong-Zhou R, Bao-Qiu C, Zhong-Yu M and Gong-Ou X 2001 *Commun. Theor. Phys.* **35** 717
[20] Hamamoto I 2010 *Phys. Rev.* C **81** 021304
[21] Urata Y, Hagino K and Sagawa H 2011 *Phys. Rev.* C **83** 041303
[22] Minomo K, Sumi T, Kimura M, Ogata K, Shimizu Y R and Yahiro M 2012 *Phys. Rev. Lett.* **108** 052503
[23] Shubhchintak and Chatterjee R 2014 *Nucl. Phys.* A **922** 99
[24] Hong J, Bertulani C A and Kruppa A T 2017 *Phys. Rev.* C **96** 064603
[25] Li J G, Michel N, Li H H and Zuo W 2022 *Phys. Lett.* B **832** 137225
[26] Hammer H-W and Phillips D R 2011 *Nucl. Phys.* A **865** 17
[27] He F 2019 *Few-Body Syst.* **60** 16
[28] Rupak G and Higa R 2011 *Phys. Rev. Lett.* **106** 222501
[29] Fernando L, Higa R and Rupak G 2012 *Eur. Phys. J.* A **48** 24
[30] Zhang X, Nollett K M and Phillips D R 2014 *Phys. Rev.* C **89** 024613
[31] Kaplan D B, Savage M J and Wise M B 1998a *Phys. Lett.* B **424** 390
[32] Kaplan D B, Savage M J and Wise M B 1998b *Nucl. Phys.* B **534** 329
[33] Hammer H W and Lee D 2009 *Phys. Lett.* B **681** 500
[34] Hammer H W and Lee D 2010 *Annals Phys.* **325** 2212
[35] Braun J, Elkamhawy W, Roth R and Hammer H-W 2019 *J. Phys.* G **46** 115101
[36] Shamsuzzoha Basunia M 2010 *Nucl. Data Sheets* **111** 2331
[37] Khersonskii V K, Moskalev A N and Varshalovich D A 1988 *Quantum Theory Of Angular Momentum* (Singapore: World Scientific Publishing Company)
[38] Fernando L, Vaghani A and Rupak G 2015 arXiv:1511.04054 [nucl-th]
[39] Zelevinsky V and Volya A 2017 Nuclear deformation *Physics of Atomic Nuclei* (Weinheim: Wiley) pp 223–50 ch 12
[40] Greiner W, Bromley D A and Maruhn J 1996 *Nuclear Models* (Berlin Heidelberg: Springer)
[41] Greiner W and Maruhn J A 1996 *Nuclear Models* (Berlin: Springer)
[42] Typel S and Baur G 2005 *Nucl. Phys.* A **759** 247
[43] Bertulani C A 2009 arXiv:0908.4307 [nucl-th]
[44] Bertulani C A and Baur G 1988 *Phys. Rep.* **163** 299
[45] Acharya B and Phillips D R 2013 *Nucl. Phys.* A **913** 103
[46] Moro A M, Lay J A and Gómez Camacho J 2020 *Phys. Lett.* B **811** 135959
[47] Ryberg E, Forssén C, Phillips D R and van Kolck U 2020 *Eur. Phys. J.* A **56** 7
[48] Papenbrock T and Weidenmüller H A 2020 *Phys. Rev.* C **102** 044324
[49] Alnamlah I K, Pérez E A C and Phillips D R 2021 *Phys. Rev.* C **104** 064311